

1 **A Combined effect of the Earth's magnetic dipole tilt**  
2 **and IMF  $B_y$  in controlling auroral electron**  
3 **precipitation**

4 **J. Laitinen<sup>1</sup>, L. Holappa<sup>1</sup>, H. Vanhamäki<sup>1</sup>**

5 <sup>1</sup>Space Physics and Astronomy Research Unit, University of Oulu, Oulu, Finland.

6 **Key Points:**

- 7 • IMF  $B_y$  and Earth's dipole tilt angle  $\Psi$  (season) modulate auroral electron pre-  
8 cipitation
- 9 • Precipitation is stronger for 13.9-30 keV at auroral latitudes on the dawnside for  
10 both hemispheres, when  $B_y$  and  $\Psi$  have opposite signs
- 11 •  $B_y$  drives a strong dawn-dusk difference for energies 1.4-6.5 keV in the summer  
12 hemisphere

---

Corresponding author: J. Laitinen, [jussi.laitinen@oulu.fi](mailto:jussi.laitinen@oulu.fi)

**Abstract**

Precipitation of auroral electrons is usually assumed to be symmetric with respect to the sign of the dawn-dusk ( $B_y$ ) component of the interplanetary magnetic field (IMF). This is also the case in most currently used precipitation models, which parameterize solar wind driving by empirical coupling functions. However, recent studies have showed that geomagnetic activity is significantly modulated by the signs and amplitudes of IMF  $B_y$  and the Earth's dipole tilt angle  $\Psi$ . This so called explicit  $B_y$  dependence is not yet included in any current precipitation models. In this paper, we quantify this  $B_y$  dependence for auroral electron precipitation for the first time. We use precipitation measurements of the Defense Meteorological Satellite Program (DMSP) Special Sensor J instruments from years 1995-2022. We show that the dawnside electron precipitation at energies 13.9-30 keV is greater at auroral latitudes for opposite signs of  $B_y$  and  $\Psi$  in both hemispheres, while the dusk sector is mostly unaffected by  $B_y$  and  $\Psi$ . For energies below 6.5 keV the  $B_y$  dependence is strong poleward of the auroral oval in the summer hemisphere, also exhibiting a strong dawn-dusk asymmetry. We also show that  $B_y$  dependence of precipitation modulates ionospheric conductance, which has important implications for solar wind response of ionospheric currents.

**Plain Language Summary**

Electron precipitation into the Earth's ionosphere creating the aurora borealis is driven by the magnetic field carried by the solar wind. The electron precipitation is known to increase the most, when the magnetic field of the solar wind points to south. The currently used models assume equally strong electron precipitation for eastward and westward solar wind magnetic fields. However, in this paper we show that the electron precipitation is different for duskward and dawnward magnetic fields, and that this magnetic field dependence varies with the season. We show that the electron precipitation is stronger on the dawnside in both hemispheres during the northern hemisphere winter when the solar wind magnetic field points duskward. In northern hemisphere summer the dependence on the magnetic field direction is opposite. We show that the solar wind magnetic field modulates the ionospheric conductivity in a similar way which has implications for ionospheric electric currents and related space weather effects on ground, such as disturbances on power lines.

## 44 1 Introduction

45 Space weather is driven by the solar wind and the interplanetary magnetic field (IMF)  
 46 driving magnetic reconnection on the dayside magnetopause. This reconnection produces  
 47 magnetospheric convection [Dungey, 1961], leading to geomagnetic activity and mod-  
 48 ulation of magnetospheric plasma populations. Accurate modelling of space weather has  
 49 multiple benefits from both societal and scientific standpoints. One great challenge of  
 50 space weather modelling is to accurately model auroral particle precipitation into the  
 51 ionosphere which, together with the solar illumination, is the main driver of ionospheric  
 52 conductance and thus fundamentally important for ionospheric dynamics.

53 *Hardy et al.* [1985] developed the first statistical precipitation model based on De-  
 54 fense Meteorological Satellite Program (DMSP) Special Sensor J (SSJ) data. The Hardy  
 55 model is parameterized by the geomagnetic  $Kp$  index. As the DMSP particle data set  
 56 has grown over the years, new models have followed [Newell et al., 2009; Zhu et al., 2021].  
 57 One example is the widely used OVATION auroral precipitation model [Newell et al.,  
 58 2014], which also takes into account seasonal variation and effects of different types of  
 59 aurora. Instead of the discrete  $Kp$  index, the OVATION model is parametrized by the  
 60 Newell coupling function [Newell et al., 2007]

$$d\Phi/dt = v^{4/3} B_T^{2/3} \sin^{8/3}(\theta/2), \quad (1)$$

61 where  $v$  is the solar wind speed,  $B_T = \sqrt{B_z^2 + B_y^2}$  and  $\theta = \arctan2(B_y/B_z)$  is the so-  
 62 called clock angle.

63 The Newell coupling function has similarities to other existing coupling functions,  
 64 predicting enhanced coupling with enhanced  $v$  and north-south ( $B_z$ ) component. While  
 65 the dawn-dusk component ( $B_y$ ) is also included, its effect is symmetric with respect to  
 66 its sign. That is, the OVATION model predicts equally strong precipitation for positive  
 67 and negative IMF  $B_y$ . However, a considerable amount of research has shown that the  
 68 sign of the IMF  $B_y$  component has an important effect in magnetospheric convection [Cow-  
 69 ley, 1981; Chisham et al., 2007; Tenfjord et al., 2015] and in geomagnetic activity, which  
 70 is more prominent during periods of high dipole tilt  $\Psi$  ( $90^\circ$  minus the angle between the  
 71 Earth's magnetic dipole axis and the Sun-Earth line). In geomagnetic activity, this ef-  
 72 fect can be summarized with a following rule: particle precipitation and geomagnetic ac-  
 73 tivity are increased, when IMF  $B_y$  and  $\Psi$  have opposite signs [Holappa et al., 2020; Reis-

74 *tad et al.*, 2020; *Ohma et al.*, 2021]. This so-called explicit  $B_y$ -effect has been shown to  
 75 modulate the westward electrojet [*Friis-Christensen and Wilhelm, 1975; Friis-Christensen*  
 76 *et al.*, 2017; *Holappa and Mursula, 2018*], size of the polar cap [*Reistad et al.*, 2020], and  
 77 the substorm occurrence rate [*Ohma et al.*, 2021]. All above studies have found  $B_y$ -effects  
 78 following the same rule, suggesting that the above effects are connected via similar phys-  
 79 ical mechanism.

80 *Holappa et al.* [2020] studied the explicit  $B_y$  dependence in energetic electron pre-  
 81 cipitation in both hemispheres using the National Oceanic and Atmospheric Adminis-  
 82 tration (NOAA) Polar-Orbiting Operational Environmental Satellites. They found that  
 83 energetic ( $>30$  keV) electron precipitation is modulated by the IMF  $B_y$  component. In  
 84 NH winter (negative  $\Psi$ ) the flux of precipitating electrons is greater for positive  $B_y$  than  
 85 for negative  $B_y$  in both hemispheres. In NH summer (positive  $\Psi$ ), the  $B_y$  dependence  
 86 is reversed. The effect was found to be strong in the midnight and dawn sectors and weak  
 87 in the dusk sector. Also, the magnitude of the  $B_y$ -effect was found to be roughly equal  
 88 in both hemispheres and solstices. If also auroral electrons (1-30 keV) would be mod-  
 89 ulated by IMF  $B_y$  in a similar way, the  $B_y$  dependence would also be significant for iono-  
 90 spheric conductance. However, the  $B_y$  dependence of auroral electron precipitation has  
 91 not been yet studied directly. Nevertheless, statistical studies of field-aligned currents  
 92 (FACs) have provided some indirect evidence [*Anderson et al.*, 2008; *Green et al.*, 2009;  
 93 *Laundal et al.*, 2018; *Holappa et al.*, 2021; *Workayehu et al.*, 2021], because the upward  
 94 FACs are known to be related to electron precipitation [e.g., *Korth et al.*, 2014].

95 None of the current precipitation models are designed to take the possible season-  
 96 ally dependent  $B_y$ -effect in auroral particle precipitation into account. The recently de-  
 97 veloped ASHLEY precipitation model [*Zhu et al.*, 2021] uses the sign of the IMF  $B_y$  com-  
 98 ponent as an input, but does not include seasonal dependence, which is crucial for  $B_y$ -  
 99 effects. A machine-learning precipitation model by *McGranaghan et al.* [2021] includes  
 100  $B_y$  as an input, but its effect on precipitation patterns has not been quantified.

101 The goal of this paper is to quantify the possible explicit IMF  $B_y$  dependence of  
 102 auroral (1-30 keV) electron precipitation, especially during periods of large dipole tilt.  
 103 We also quantify the  $B_y$  dependence on ionospheric conductance and discuss its impli-  
 104 cations to geomagnetic activity. This is done by utilizing the database of DMSP SSJ par-

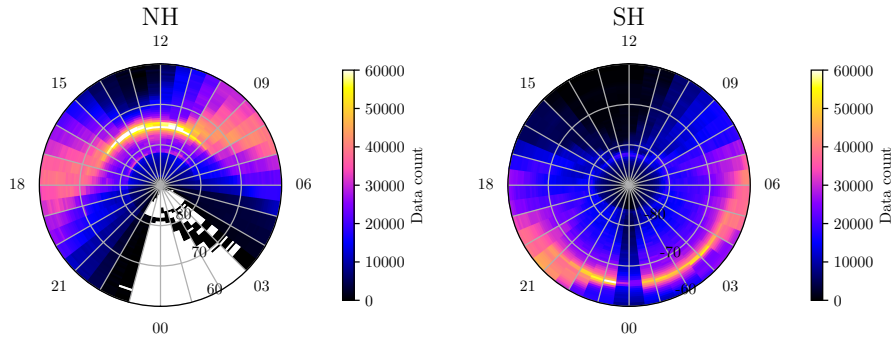
105 ticle data from years 1995-2022, which is also the basis for several existing precipitation  
106 models.

107 This paper is organized as follows. In Section 2 we present the general properties  
108 of the DMSP satellites and their instruments measuring the precipitating particles, and  
109 go through the data processing techniques forming the results. In Section 3 we show the  
110  $B_y$ -effect in the measured differential number flux and in the calculated total energy flux  
111 and average energy. Also, we show the  $B_y$ -effect in the calculated Hall conductance. In  
112 Section 4 we discuss how the results affect the modern precipitation models, and how  
113 the results compare to the recent literature of the  $B_y$ -effect. Finally we present our con-  
114 clusions in Section 5.

## 115 2 Data and Methods

### 116 2.1 DMSP Particle Data

117 In this study we use DMSP particle data from years 1995-2022, from DMSP satel-  
118 lites F10 through F19 (with F19 covering only years 2014-2016). DMSP satellites fly in  
119 circular, sun-synchronous polar orbits (inclination  $98.8^\circ$ ) at an altitude of roughly 850  
120 km. The orbits are predominantly confined to the dawn-dusk sector. However, the satel-  
121 lites jointly cover most magnetic local times (MLTs) at high geomagnetic latitudes (MLAT)  
122 in altitude adjusted corrected geomagnetic (AACGM) coordinates, but the MLT-MLAT  
123 coverage has hemispheric differences, due to hemispheric differences in the structure of  
124 the Earth's magnetic field. The satellites carry a Special Sensor for Precipitating Par-  
125 ticles versions 4 (SSJ/4) and 5 (SSJ/5) that measure fluxes of downward precipitating  
126 auroral electrons and ions [Hardy *et al.*, 2008; Redmon *et al.*, 2017]. The SSJ/4 points  
127 upwards and measures electrons and ions with energies from roughly 30 eV to 30 keV  
128 in 19 logarithmically-spaced energy bins, resulting in full electron and ion spectra ev-  
129 ery second. SSJ/4 instruments are used in this study with satellites F10-F15. The SSJ/5  
130 instrument is an updated version of SSJ/4. The difference is that it measures the incom-  
131 ing flux of particles from a range of angles (from  $4^\circ$  to  $90^\circ$ ), divided into six  $15^\circ$  angu-  
132 lar sectors. However, due to constraints in telemetry, the counts from different angular  
133 sectors are averaged, resulting one spectrum every second (similarly as in SSJ/4). Due  
134 to these instrumental differences, there may be some systematic differences between the  
135 fluxes measured by SSJ/4 and SSJ/5. For instance, the larger field of view of the SSJ/5



144 **Figure 1.** Data count of DMSP particle measurements from years 1995-2022 for northern  
 145 (NH) and southern hemispheres (SH) after sorting the data with the criteria: IMF  $|B_y| > 2$   
 146 nT, the Earth's dipole tilt angle  $|\Psi| > 15^\circ$ , and the normalized Newell coupling function  
 147  $1 < d\Phi/dt / \langle d\Phi/dt \rangle < 2$ .

136 can result into measurement of electrons outside the loss cone, if the satellite is in the  
 137 ascending phase [Redmon *et al.*, 2017]. However, the observed IMF  $B_y$  dependencies stud-  
 138 ied in this paper did not show systematic differences between SSJ/4 and SSJ/5, thus en-  
 139 couraging us to combine the data from both instruments to achieve the best possible data  
 140 coverage. Also, the SSJ/4 and SSJ/5 data have been combined in previous studies [Wing  
 141 *et al.*, 2013; Newell *et al.*, 2014; McGranaghan *et al.*, 2015]. All the satellites used in this  
 142 study had the ascending nodes on the dusk side.

## 143 2.2 Data Processing

148 The DMSP particle measurements are spatially binned into an MLT-latitude grid  
 149 with a grid size of 0.5 h MLT by  $0.5^\circ$  MLAT, from  $60^\circ$  to  $90^\circ$ . Figure 1 shows the data  
 150 coverage of the DMSP measurements in the northern and southern hemispheres of the  
 151 data used in this study. That is, after sorting the data with solar wind criteria IMF  $|B_y| >$   
 152  $2$  nT and the normalized Newell coupling function  $1 < d\Phi/dt / \langle d\Phi/dt \rangle < 2$  (see Sec-  
 153 tion 3.1), and large Earth's dipole tilt angles  $|\Psi| > 15^\circ$ .

154 Each MLT-MLAT bin contains the mean value of the differential number fluxes.  
 155 Due to the heavy-tailed distribution of the differential particle flux, the mean is some-  
 156 times significantly affected by outliers. The effect of outliers is alleviated with the fol-  
 157 lowing automatic procedure. First, all the bins are checked for outliers by standardiz-  
 158 ing the differential number fluxes in the bin. The potential outliers are removed from

159 the bin, if their standardized  $z$ -score is larger than  $6\sigma$  and the value is larger than  $10^4$  ( $1/\text{cm}^2\text{s} \cdot \text{eV} \cdot \text{sr}$ ).  
 160 These criteria were found to eliminate most effects of outliers.

161 The total energy fluxes are calculated from the DMSP data from all of the 19 chan-  
 162 nels for each MLT-latitude bin from the outlier removed (first procedure) differential num-  
 163 ber fluxes. Total energy fluxes are calculated with equation [Hardy *et al.*, 2008]

$$\begin{aligned}
 JE_{TOT}(\Omega) = & E_1 j(E_1, \Omega)(E_2 - E_1) + \sum_{i=2}^{18} E_i j(E_i, \Omega) \frac{E_{i+1} - E_{i-1}}{2} \\
 & + E_{19} j(E_{19}, \Omega)(E_{19} - E_{18}),
 \end{aligned} \tag{2}$$

164 where  $i$  is the channel index (from high to low),  $E_i$  is the channel central energy of chan-  
 165 nel  $i$  and  $j(E_i, \Omega)$  is the directional-differential number flux (for further theoretical ba-  
 166 sis see, e.g., Redmon *et al.* [2017]). The total number fluxes  $J_{TOT}(\Omega)$  are calculated in  
 167 a similar manner, only replacing the  $E_i j(E_i, \Omega)$  (directional-differential energy flux) term  
 168 with  $j(E_i, \Omega)$ . The average energy for each bin is calculated as

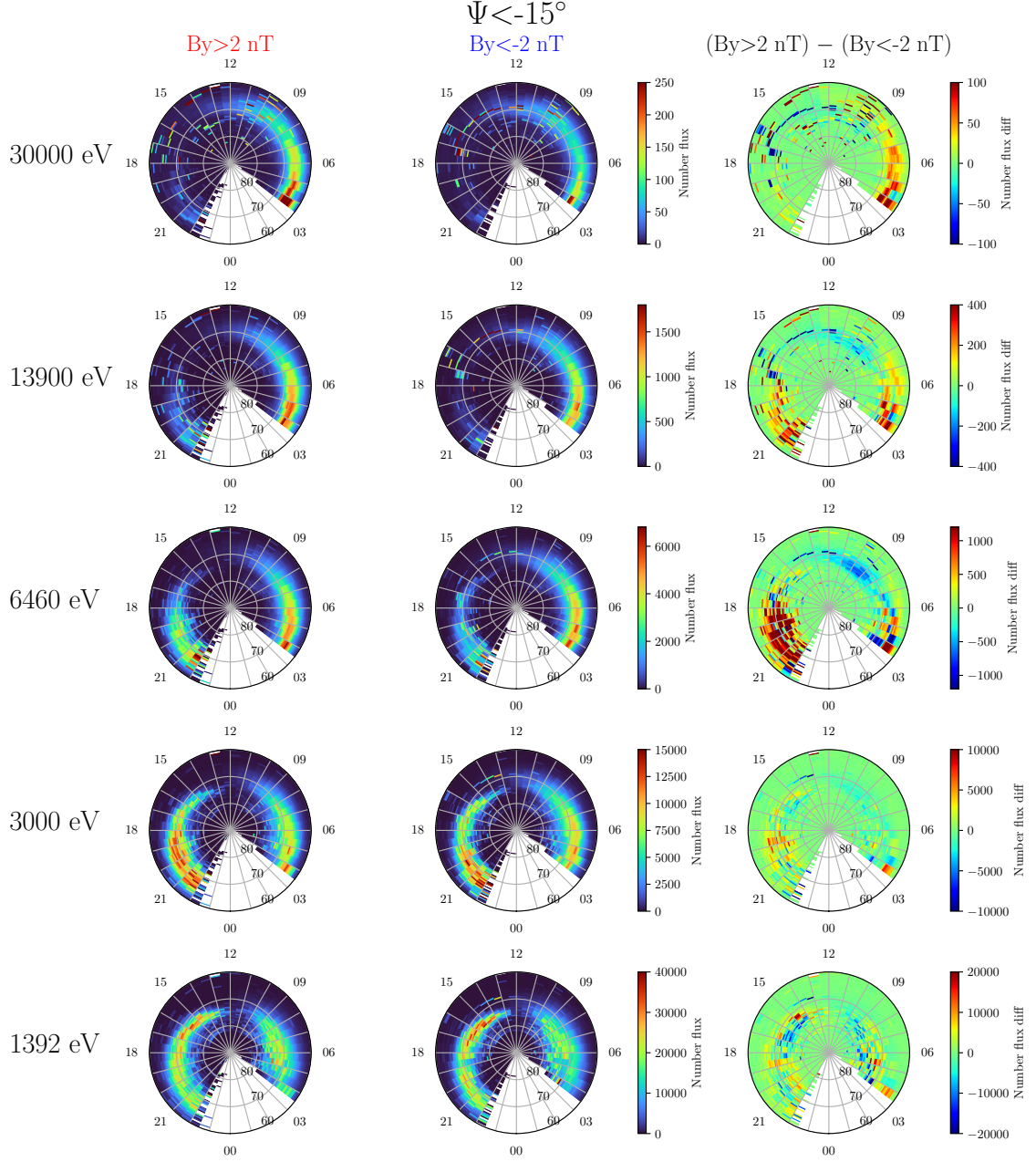
$$E_{AVE} = \frac{JE_{TOT}(\Omega)}{J_{TOT}(\Omega)}. \tag{3}$$

169 Assuming isotropic pitch-angle distribution at DMSP altitude, we calculate the down-  
 170 going total energy flux by multiplying  $JE_{TOT}(\Omega)$  by  $\pi$  [Newell *et al.*, 2014]. The calcu-  
 171 lated down-going total energy flux and the average energy are used to calculate the Hall  
 172 conductance for each bin using the Robinson formulas [Robinson *et al.*, 1987] to show  
 173 the potential  $B_y$ -effect of auroral precipitation on ionospheric conductivity. The Robin-  
 174 son formulas are defined as

$$\Sigma_P = \frac{40E_{AVE}}{16 + (E_{AVE})^2} (JE_{TOT})^{1/2} \tag{4}$$

$$\frac{\Sigma_H}{\Sigma_P} = 0.45(E_{AVE})^{0.85}, \tag{5}$$

175 where the  $\Sigma_P$  and  $\Sigma_H$  Pedersen and Hall conductances. The average energy  $E_{AVE}$  is  
 176 in units of keV and the down-going total energy flux  $JE_{TOT}$  in  $\text{ergs}/\text{cm}^2\text{s}$ .



179 **Figure 2.** Precipitation map of the differential number fluxes ( $1/\text{cm}^2\text{s} \cdot \text{eV} \cdot \text{sr}$ ) in the north-  
 180 ern hemisphere with dipole tilt  $\Psi < -15^\circ$  (local winter) for five channels. The channel central  
 181 energies are shown on the left for each row. The first two columns show the differential number  
 182 fluxes, when the IMF  $B_y > 2$  nT and  $B_y < -2$  nT, and the third column shows the difference  
 183 of these two precipitation maps. The maps cover MLATs from  $60^\circ$  to  $90^\circ$ . A large gap in data  
 184 exists from 22 to 04 MLT.

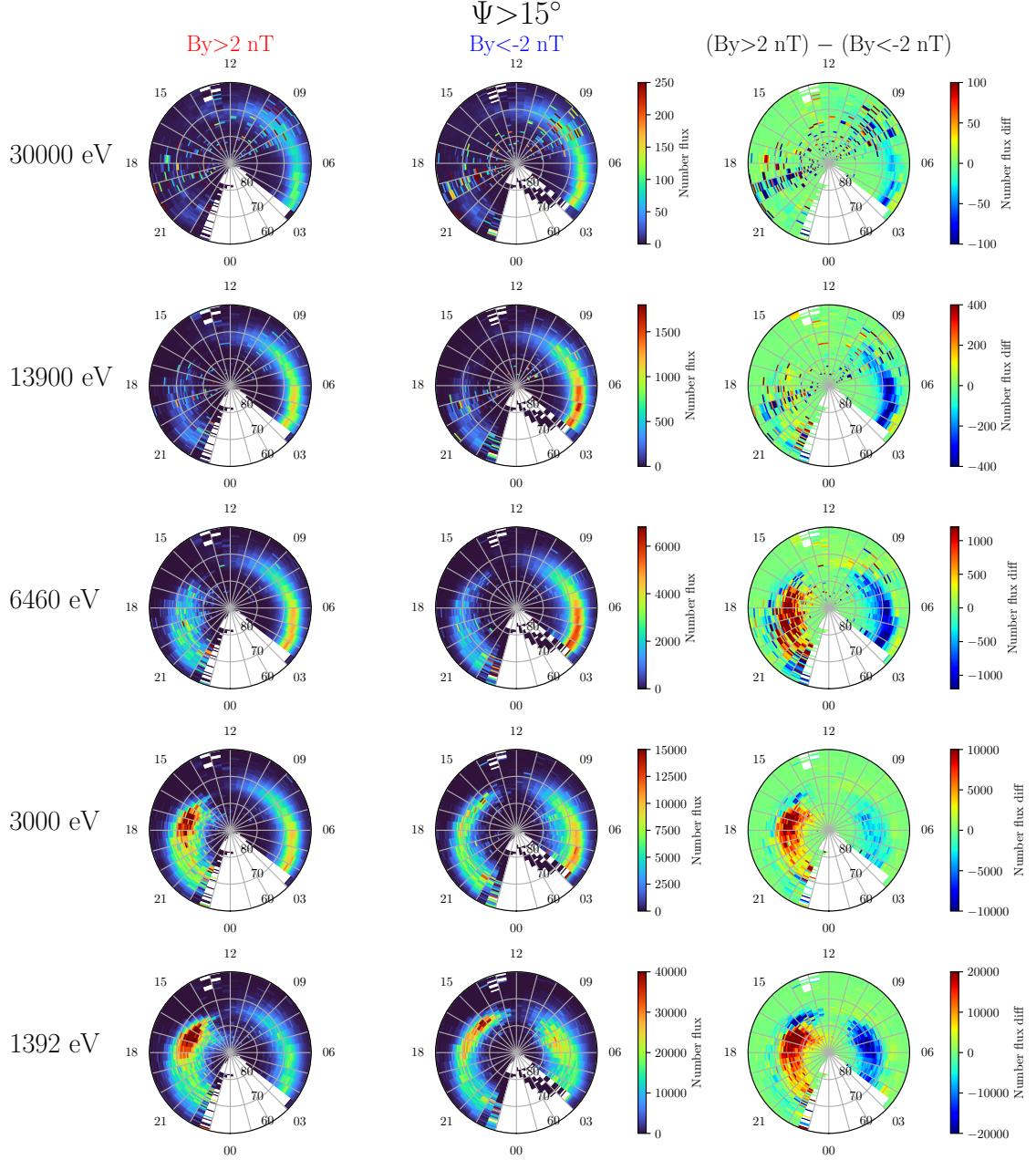
### 3 Results

#### 3.1 Differential number flux

For quantifying IMF  $B_y$  dependence of precipitation, we sort the DMSP data with IMF  $B_y$  and the Newell coupling function, averaged over the current and three previous UT hours. The Newell function is normalized by its mean  $\langle d\Phi/dt \rangle$  in 1995-2022. Figure 2 shows a map of the differential number flux ( $1/\text{cm}^2\text{s} \cdot \text{eV} \cdot \text{sr}$ ) in the northern hemisphere (NH) for dipole tilt  $\Psi < -15^\circ$  (local winter). In all panels the normalized Newell coupling function  $d\Phi/dt/\langle d\Phi/dt \rangle$  is limited between 1 and 2. Thus, all panels correspond to solar wind driving slightly stronger than the long-term mean. Because the DMSP satellites are primarily on dawn-dusk orbits, there is no data coverage in the NH at 22-04 MLT and very limited data at 12-15 MLT between  $60^\circ$ - $70^\circ$  MLAT (see Figure 1). Each row displays a different energy channel labeled by nominal central energies of the channels. Precipitation maps are shown for five channels, showing every other channel starting from the highest channel (30 keV). Thus, to shorten the text, from here on out we reference these channels as 30 keV, 13.9 keV, 6.5 keV, 3 keV, and 1.4 keV. The first two columns show the differential number fluxes during positive ( $> 2$  nT) and negative  $B_y$  ( $< -2$  nT), respectively, and the third column shows their difference. The first and second columns show that the amount of precipitation changes drastically between the energy channels. The precipitation patterns in the highest energy channels (30 keV and 13.9 keV) show strong dawn-dusk differences and the maximum precipitation region is located close to the auroral oval, while the lower channels show more dawn-dusk symmetric distributions, which extend poleward of the auroral oval.

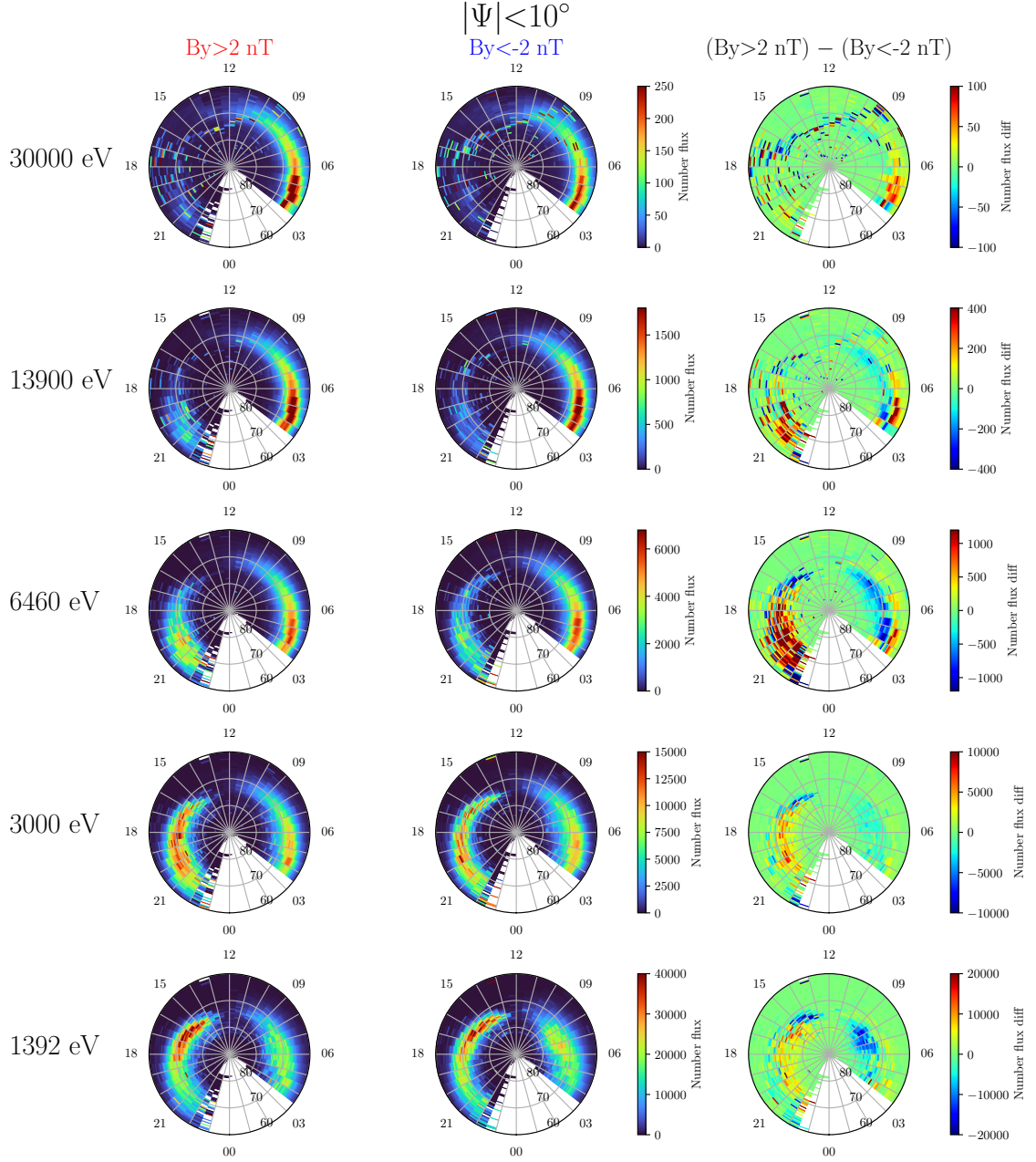
Figure 2 (especially the third column) shows a clear  $B_y$  dependence for the highest energy channels (30 and 13.9 keV). The number fluxes are higher for  $B_y > 2$  nT, especially on the dawnside auroral oval (at 60-70 MLAT). This effect can be seen in the 6.5 keV energy channel as well, but not as clearly. The 3 keV channel shows only weak  $B_y$  dependence and the 1.4 keV channel shows no systematic  $B_y$ -effect.

Figure 3 shows the precipitation map in NH for  $\Psi > 15^\circ$  (NH summer) in a similar format as Figure 2. The  $B_y$  dependence during positive tilt (quantified in the third column) is clearly opposite to that during negative tilt (Figure 2), in agreement with the earlier results on the  $B_y$  dependence of high energy precipitation [Holappa *et al.*, 2020]. The number fluxes are greater for  $B_y < -2$  nT than for  $B_y > 2$  nT on the dawn side



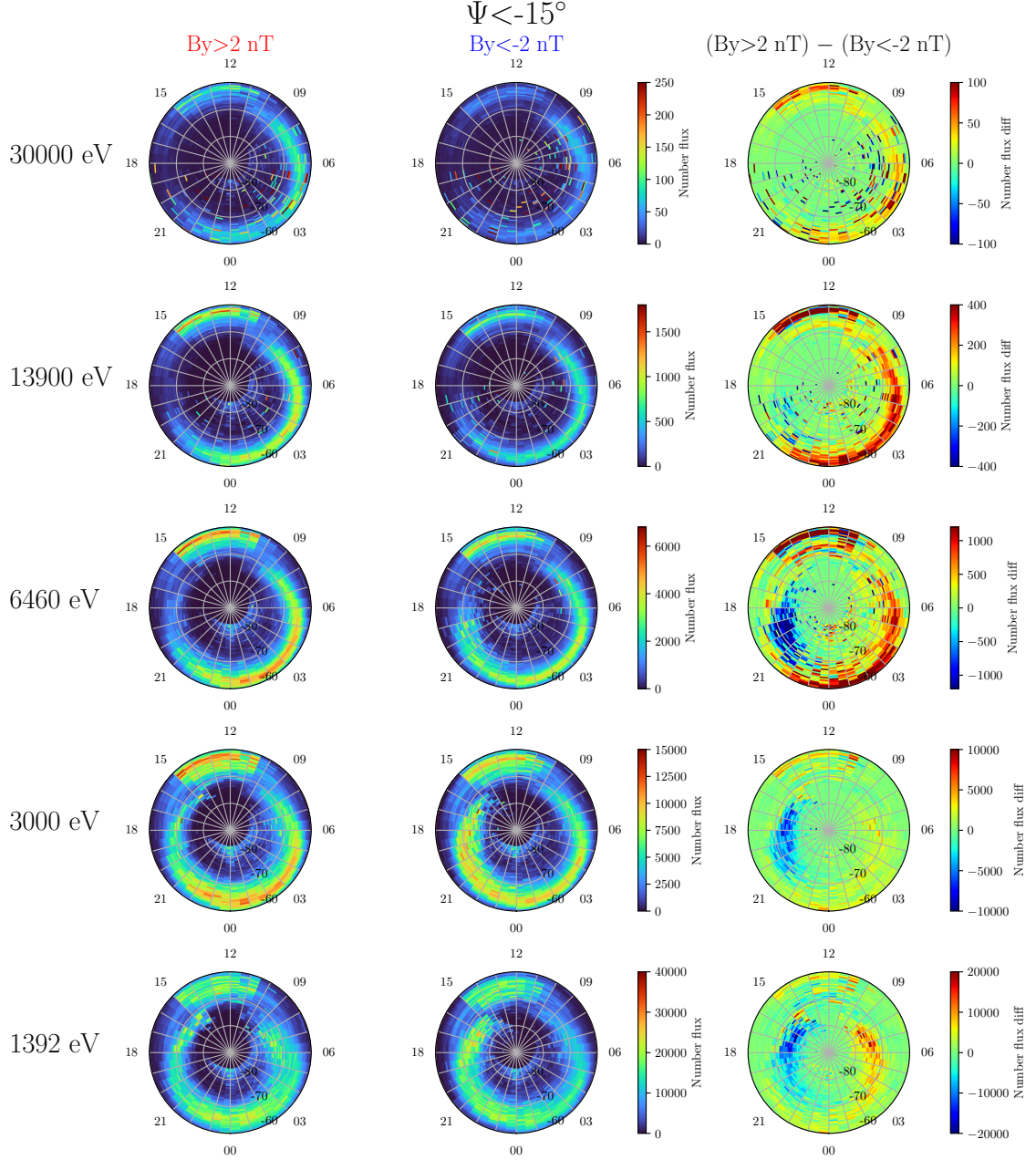
210 **Figure 3.** Precipitation map of the differential number fluxes ( $1/\text{cm}^2\text{s} \cdot \text{eV} \cdot \text{sr}$ ) in the north-  
 211 ern hemisphere with dipole tilt  $\Psi > 15^\circ$  (local summer) in similar format as in Figure 2.

217 in all channels. There are, however, also other differences between summer and in win-  
 218 ter precipitation patterns: a strong dawn-dusk difference is seen in channels 6.5 keV, 3  
 219 keV and 1.3 keV, so that the number fluxes increase on the dawnside during  $B_y < -2$   
 220 nT and on the duskside during  $B_y > 2$  nT. The  $B_y$ -effect is seen to extend to higher  
 221 latitudes with decreasing energies.



222 **Figure 4.** Precipitation map of the differential number fluxes ( $1/\text{cm}^2\text{s} \cdot \text{eV} \cdot \text{sr}$ ) in the north-  
 223 ern hemisphere with dipole tilt  $|\Psi| < 10^\circ$  (neutral tilt) in similar format as in Figure 2.

224 Figure 4 shows the precipitation map in NH for  $|\Psi| < 10^\circ$  (neutral tilt). The  $B_y$   
 225 dependence varies between the higher and lower channels. The 30 keV channel shows  
 226 greater number fluxes for  $B_y > 2$  nT at dawnside auroral latitudes similar to Figure  
 227 2, but weaker. However, channel 13.9 keV shows unclear  $B_y$  dependence on the dawn-  
 228 side, but greater number fluxes on the duskside for  $B_y > 2$  nT. Channels 3 keV and



231 **Figure 5.** Precipitation map of the differential number fluxes ( $1/\text{cm}^2 \cdot \text{s} \cdot \text{eV} \cdot \text{sr}$ ) in the south-  
 232 ern hemisphere with dipole tilt  $\Psi < -15^\circ$  (local summer) in similar format as in Figures 2-4.

229 1.4 keV display similar, but much weaker  $B_y$  dependence seen for NH summer in Fig-  
 230 ure 3.

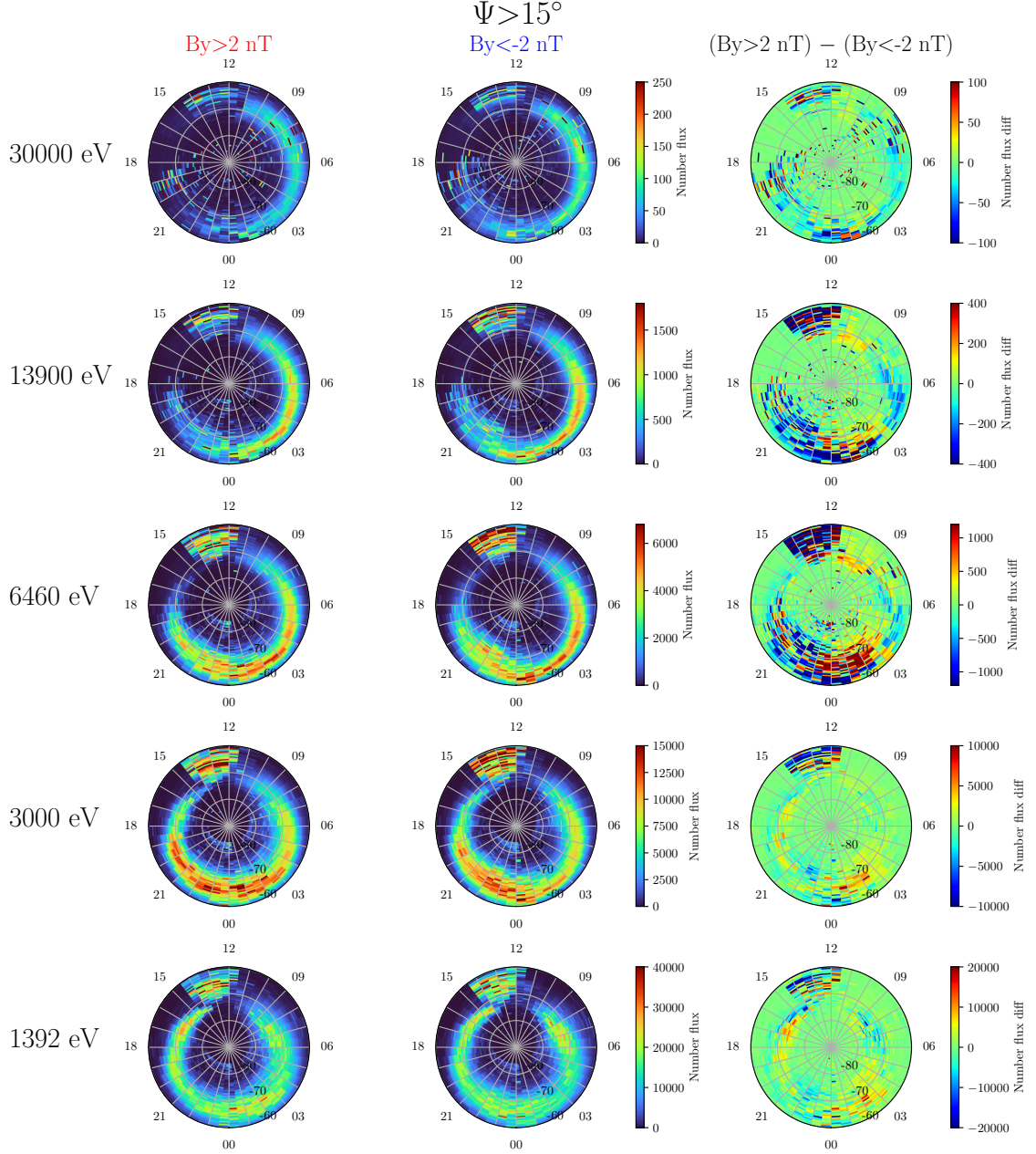
233 Figure 5 shows the precipitation map of the differential number flux in the south-  
 234 ern hemisphere (SH) with dipole tilt  $\Psi < -15^\circ$  (SH summer). The notable difference

235 to the northern hemisphere (Figure 3) is the better MLT-MLAT coverage. However, the  
 236 data coverage is poor at the dayside between 10-15 MLT (Figure 1), which produces clear  
 237 anomalies in all panels. In the first two columns, channels from 6.5 keV to 30 keV show  
 238 similar precipitation patterns maximizing at the auroral latitudes between 21 and 09 MLT.  
 239 In the lower energy channels precipitation extends roughly from 17 MLT to 09 MLT. The  
 240 third column shows a clear  $B_y$  dependence for energies between 6.5 keV and 30 keV. The  
 241 number fluxes are clearly greater for  $B_y > 2$  nT at 22-09 MLT. The effect is in the same  
 242 direction as in the NH local summer, implying it is from the same, global physical mech-  
 243 anism. Channels between 1.4-6.5 keV show increased number fluxes in the duskside, and  
 244 the channel 3 keV does not show as clear increase of dawnside number fluxes during  $B_y >$   
 245 2 nT. The channel 1.4 keV shows a high latitude dawn-dusk difference, which is oppo-  
 246 site and weaker to that in NH summer (Figure 3).

249 Figure 6 shows the precipitation map in SH during  $\Psi > 15^\circ$  (SH winter). The num-  
 250 ber fluxes are generally slightly larger overall than in SH summer (Figure 5). A  $B_y$  de-  
 251 pendence is also seen in the highest energy channels (30 keV and 13.9 keV) at dawn and  
 252 pre-midnight sectors, but it is weaker than in SH summer. Channels from 6.5 keV to 1.4  
 253 keV do not show a clear  $B_y$ -effect.

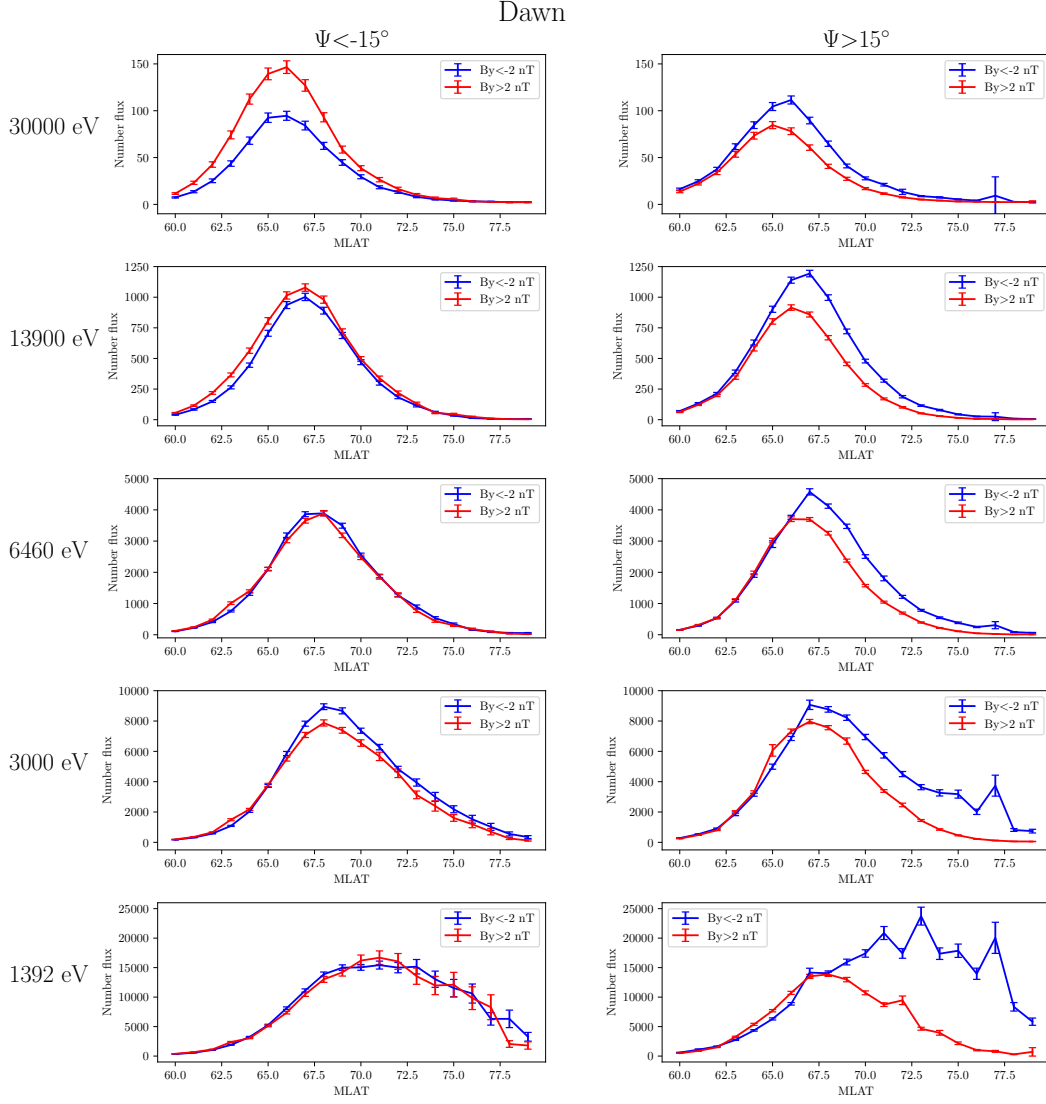
257 Comparing the above results from the two hemispheres we can summarize that at  
 258 the dawn sector auroral latitudes precipitation increases for opposite signs of IMF  $B_y$   
 259 and  $\Psi$  in both hemispheres. However, the  $B_y$  dependence is stronger in the summer hemi-  
 260 sphere. In the summer hemisphere IMF  $B_y$  drives a clear dawn-dusk asymmetry in high-  
 261 latitude ( $> 70^\circ$ ) precipitation. This effect is most clear for the lowest energy (1.4 keV)  
 262 for which the precipitation patterns during positive and negative  $B_y$  are almost mirror  
 263 images of each other. This "mirroring" is seen best in the SH (Figure 5), where the MLT  
 264 coverage is better than in the NH.

268 To further quantify the  $B_y$  dependence in the NH at dawn, Figure 7 shows a merid-  
 269 ional cut at 05-07 MLT of the differential number fluxes from Figures 2 and 3 together  
 270 with their standard errors. The dawside precipitation shows larger number fluxes for  $B_y >$   
 271 2 nT than for  $B_y < -2$  nT for 30 keV during  $\Psi < -15^\circ$ . However, 3 keV shows slightly  
 272 larger number fluxes for  $B_y < -2$  nT than for  $B_y > 2$  nT. Other energies show only  
 273 small or no clear  $B_y$ -effect. During  $\Psi > 15^\circ$  the number fluxes are larger and peak roughly  
 274  $0.5^\circ$  MLAT poleward for  $B_y < -2$  nT than for  $B_y > 2$  nT for energies between 6.5



247 **Figure 6.** Precipitation map of the differential number fluxes ( $1/\text{cm}^2\text{s} \cdot \text{eV} \cdot \text{sr}$ ) in the south-  
 248 ern hemisphere with dipole tilt  $\Psi > 15^\circ$  (local winter) in similar format as in Figures 2-6.

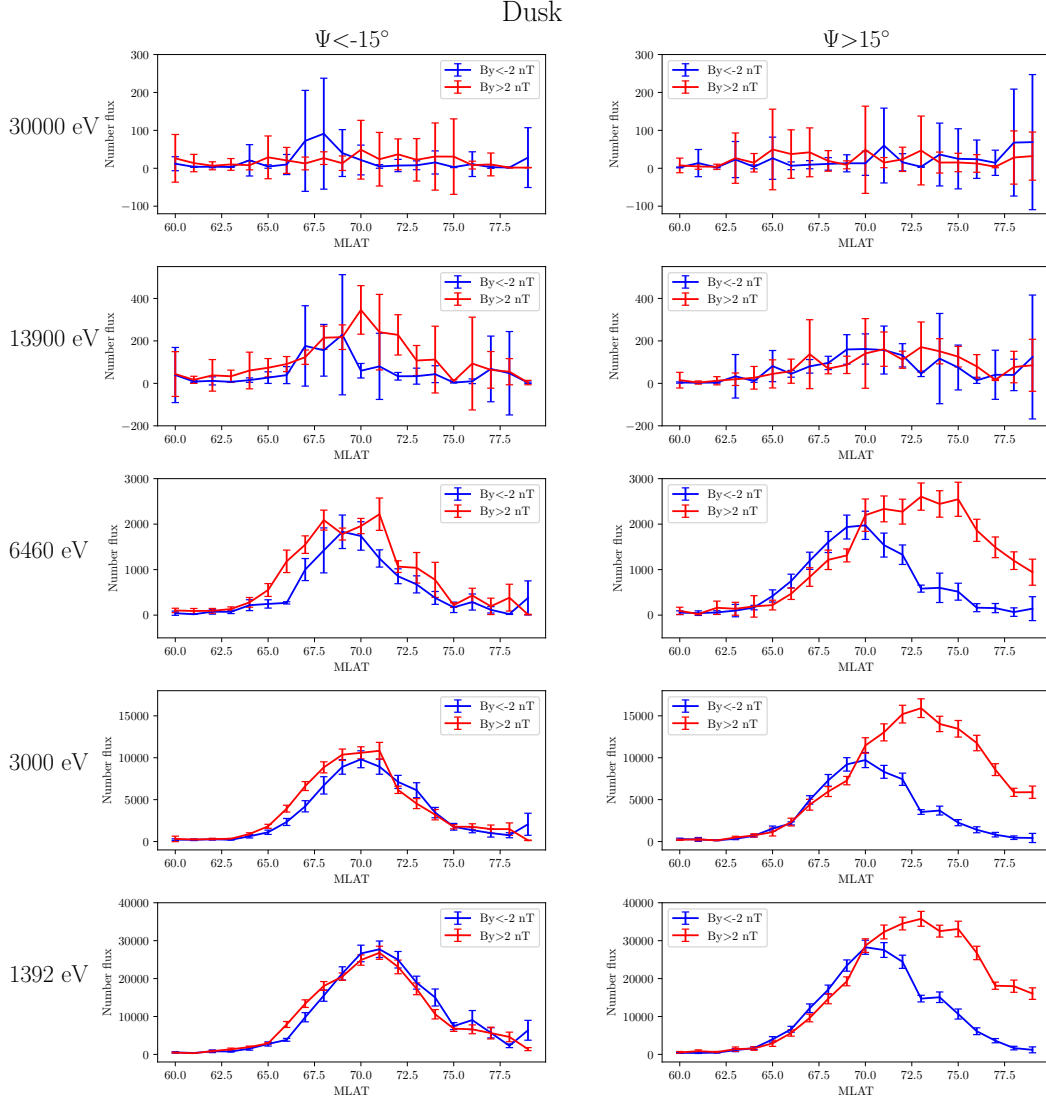
275 keV and 30 keV. Energies 1.4 keV and 3 keV show number fluxes extending to higher  
 276 latitudes with decreasing energies. The number fluxes at dusk (17-19 MLT, Figure 8)  
 277 show only slightly larger number fluxes for  $B_y > 2$  nT than for  $B_y < -2$  nT during  
 278  $\Psi < -15^\circ$  for energies between 3 keV and 13.9 keV. However, during  $\Psi > 15^\circ$  ener-



254 **Figure 7.** Northern hemisphere dawnside differential number fluxes ( $1/\text{cm}^2\text{s} \cdot \text{eV} \cdot \text{sr}$ ) from  
 255 sector 05-07 MLT shown with error bars for winter ( $\Psi < -15^\circ$ ) and summer ( $\Psi > 15^\circ$ ). Red line  
 256 corresponds to number fluxes during IMF  $B_y > 2$  nT and blue line during  $B_y < -2$  nT.

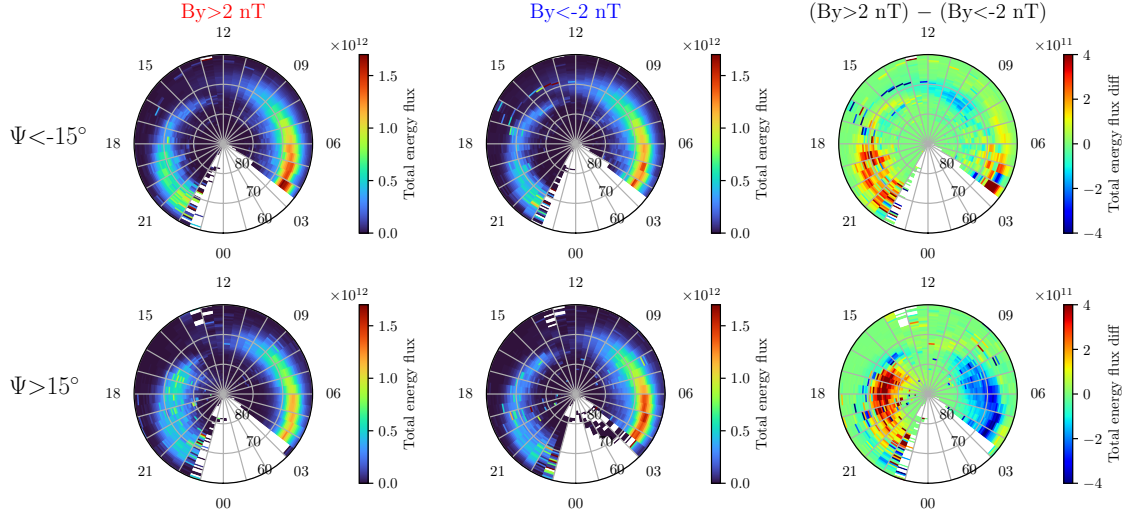
279 gies from 1.4 keV and 6.5 keV show larger number fluxes that extend to higher latitudes  
 280 for  $B_y > 2$  nT than for  $B_y < -2$ .

281 In the calculation of the standard errors  $\sigma/\sqrt{N}$  we used the number of orbits as  
 282 the factor  $N$ . This ensures that we treat only measurements made during different or-  
 283 bits as statistically independent from each other. As seen in Figure 7, errorbars at the  
 284 dawnside stay relatively small, indicating that the results are statistically reliable. How-  
 285 ever, Figure 8 shows much larger errorbars for 30 keV and 13.9 keV channels for both



265 **Figure 8.** Northern hemisphere duskside differential number fluxes ( $1/\text{cm}^2\text{s} \cdot \text{eV} \cdot \text{sr}$ ) from  
 266 sector 17-19 MLT shown with error bars for summer ( $\Psi > 15^\circ$ ) and winter ( $\Psi < -15^\circ$ ). Red line  
 267 corresponds to number fluxes during IMF  $B_y > 2$  nT and blue line during  $B_y < -2$  nT.

286 tilt angles at dusk, while 6.5 keV, 3 keV, and 1.4 keV channels show relatively small er-  
 287 rorbars for both tilt angles, comparable to ones in the dawn side in Figure 7. Therefore,  
 288 the relatively high uncertainties should be kept in mind when interpreting the high-energy  
 289 part of dusk precipitation (30 keV and 13.9 keV) in Figures 2 and 3.

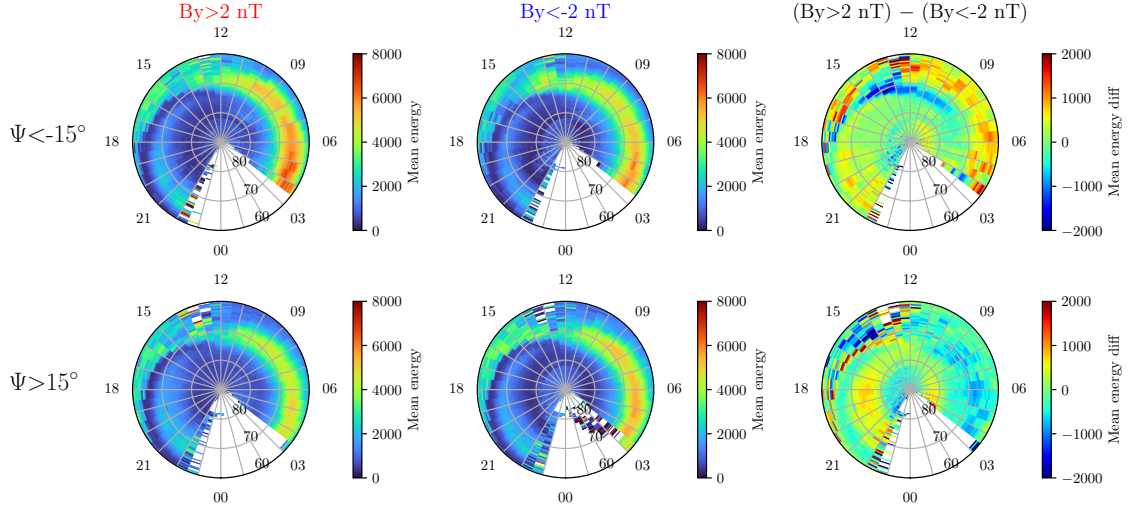


291 **Figure 9.** Total energy fluxes ( $\text{eV}/\text{cm}^2\text{s}\cdot\text{sr}$ ) for the northern hemisphere. The first row are  
 292 the total energies for tilt angle  $\Psi < -15^\circ$  and the second row for tilt angle  $\Psi > 15^\circ$ . First column  
 293 shows the total energies for IMF  $B_y > 2$  nT, second row for  $B_y < -2$  nT, and the third row the  
 294 difference of the two total energy flux maps.

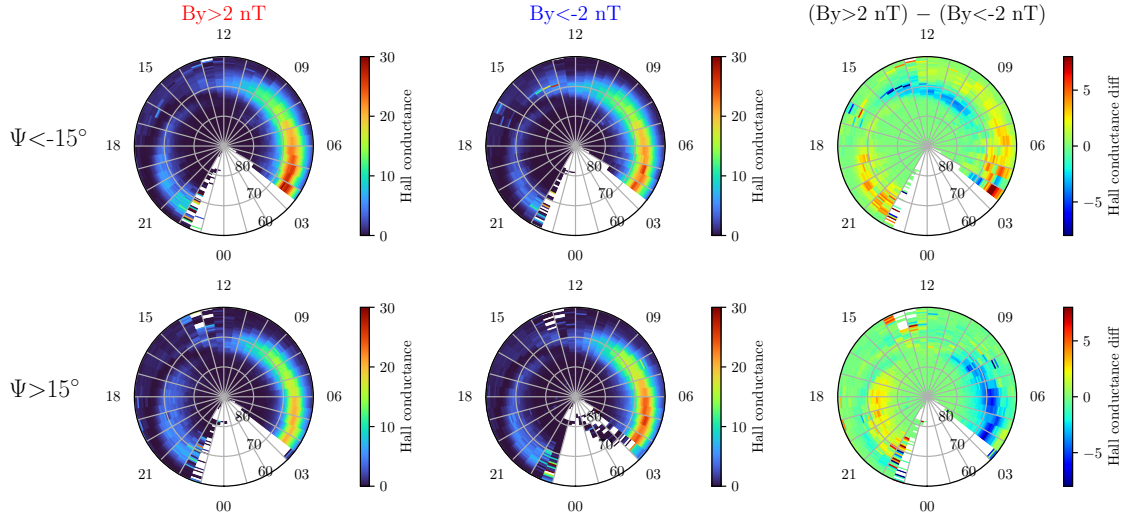
### 290 3.2 Total energy flux, average energy and ionospheric conductivity

295 Figure 9 shows the total energy fluxes for the NH calculated with Equation (2) for  
 296  $\Psi < -15^\circ$  in the first row and  $\Psi > 15^\circ$  in the second in a similar format as Figures  
 297 1-4. Figure 9 shows similar  $B_y$  dependencies as Figures 2 and 3. During  $\Psi < -15^\circ$  the  
 298 total energy fluxes are generally larger for IMF  $B_y > 2$  at both dawn and dusk. How-  
 299 ever, for  $\Psi > 15^\circ$  IMF  $B_y$  drives a clear dawn-dusk asymmetry in energy fluxes with  
 300 higher dawn (dusk) energy flux for  $B_y < -2$  ( $B_y > 2$ ) nT. The  $B_y$ -effect during  $\Psi >$   
 301  $15^\circ$  is seen at higher latitudes than for  $\Psi < -15^\circ$ . This is due to the effect of  $\Psi$  onto  
 302 the particle precipitation measured by the lower energy channels, as seen in Figure 3.  
 303 Figure S1 in the Supplement shows the total energy fluxes for the SH in a similar for-  
 304 mat.

307 Figure 10 shows the average energy (eV) for the NH in a format similar to Figure  
 308 9. When the tilt angle  $\Psi$  and IMF  $B_y$  have opposite signs, the average energy increases  
 309 on the dawnside. During  $\Psi > 15^\circ$ , the average energies also only show weak dawn-dusk  
 310 difference compared to Figure 9. Also, the average energy increases in only slightly higher



305 **Figure 10.** Average energies (eV) for the northern hemisphere, in a similar format as in Fig-  
 306 ure 9.



313 **Figure 11.** Calculated Hall conductances (S) for the northern hemisphere, in a similar format  
 314 as in Figure 9 and 10. The conductances were calculated using the Robinson formulas.

311 latitudes in the duskside during  $B_y > 2$  nT, than in the dawnside during  $B_y < -2$   
 312 nT. Figure S2 in the Supplement shows the average energy for the SH.

315 The total energy flux and average energy are known to directly affect the ionospheric  
 316 Hall and Pedersen conductances. This relation is described by the Robinson formulas  
 317 given in Eqs. (4-5). Figure 11 shows the Hall conductances (in Siemens) calculated from  
 318 the total energy flux and average energy, in a similar format as Figures 9 and 10. Dur-

319 ing  $\Psi < -15^\circ$  the Hall conductance is increased with  $B_y > 2$  nT, similarly as the to-  
 320 tal energy flux and average energy in Figures 9 and 10. During  $\Psi > 15^\circ$  the Hall con-  
 321 ductance is greater for  $B_y < -2$  nT at dawn and for  $B_y > 2$  nT at dusk. However,  
 322  $\Psi > 15^\circ$  shows only weak dawn-dusk difference between  $B_y > 2$  nT and  $B_y < -2$   
 323 nT. Also, as the  $B_y$ -effect in precipitation is seen in higher latitudes during  $\Psi > 15^\circ$   
 324 than during  $\Psi < -15^\circ$ , the Hall conductance shows similar effect. Many studies have  
 325 shown that the variability of the westward electrojet is mainly controlled by variations  
 326 of the Hall conductance (rather than the electric field) [e.g., *Sugino et al.*, 2002; *Sergeev*  
 327 *et al.*, 2018]. Therefore, the result here implies that the conductance would enhance the  
 328 westward electrojet more during  $\Psi > 15^\circ$  and  $B_y < -2$  nT, and during  $\Psi < -15^\circ$   
 329 and  $B_y > 2$  nT.

#### 330 4 Discussion

331 Figures 2-6 show that auroral electron precipitation at 1-30 keV energies clearly  
 332 depends on the combination of IMF  $B_y$  direction and dipole tilt angle  $\Psi$ . We found that  
 333 the energetic part (13.9-30 keV) of the auroral precipitation at the dawn sector is greater  
 334 for opposite signs of IMF  $B_y$  and  $\Psi$  in both hemispheres, in a similar way as found in  
 335  $> 30$  keV electrons in *Holappa et al.* [2020]. However, the  $B_y$  dependence of auroral elec-  
 336 trons is more prominent in the summer hemisphere.

337 For less energetic part of auroral precipitation (below 6.5 keV) IMF  $B_y$  dependence  
 338 is somewhat different. Figures 3 and 5 show a strong dawn-dusk asymmetry between pos-  
 339 itive and negative  $B_y$  poleward of the auroral oval in the summer hemisphere. This dawn-  
 340 dusk difference is almost mirrored in the 1.4 keV precipitation patterns. In the NH,  $B_y$   
 341 is found to increase the dawnside precipitation for  $B_y < -2$  nT and duskside for  $B_y >$   
 342  $2$  nT. In the SH, this  $B_y$ -effect is seen in the opposite direction.

343 The dawnside (diffuse electron) precipitation is known to be mostly due to wave-  
 344 particle interactions between electrons and whistler-mode waves resulting into pitch an-  
 345 gles scattering of bouncing electrons [*Li et al.*, 2009; *Thorne et al.*, 2010]. However, also  
 346 broadband accelerated electron precipitation is found to peak at prenoon [*Newell et al.*,  
 347 2009]. Whistler-mode waves are known to originate from non-isotropic 10-30 keV elec-  
 348 trons injected into the inner magnetosphere during substorms [*Tsurutani and Smith*, 1974;  
 349 *Li et al.*, 2010]. Also, substorms are known to increase the diffuse electron precipitation

350 on the dawnside [*Wing et al.*, 2013]. Thus, it is probable that the IMF  $B_y$  modulates  
 351 the energetic (13.9-30 keV) dawnside precipitation via occurrence rate of substorms, be-  
 352 cause substorm occurrence rate is found to show similar  $B_y$  dependence [*Ohma et al.*,  
 353 2021]. This is supported by Figure 10, which shows that the average energy of precip-  
 354 itating electrons increases on dawnside, probably due to injected energetic electrons by  
 355 increased frequency of substorms.

356 The duskside precipitation is known to consist mostly of monoenergetic electrons,  
 357 accelerated due to field-aligned potential differences [*Newell et al.*, 2009]. These accel-  
 358 erated electrons are known to be often confined within the upward (R1) FAC in the dusk-  
 359 to-midnight sector [*Ohtani et al.*, 2010; *Korth et al.*, 2014]. The  $B_y$  dependence of these  
 360 FACs has been studied in the past [*Weimer*, 2001; *Anderson et al.*, 2008; *Tenfjord et al.*,  
 361 2015; *Laundal et al.*, 2018; *Workayehu et al.*, 2021]. The duskside R1 FAC is known to  
 362 shift and expand into higher latitudes for positive  $B_y$  in the NH summer and for neg-  
 363 ative  $B_y$  in the SH summer [*Green et al.*, 2009; *Holappa et al.*, 2021]. This is similar to  
 364 the  $B_y$ -effect in the low-energy part ( $< 6.5$  keV) of duskside precipitation in Figures 3  
 365 and 5. The precipitation patterns of 1.4 keV electrons in the summer hemisphere for pos-  
 366 itive and negative IMF  $B_y$  are almost mirror images of each other, which could be ex-  
 367 plained by the dawn-dusk asymmetry of FACs due to asymmetric magnetospheric con-  
 368 vection driven by IMF  $B_y$  [*Cowley*, 1981; *Tenfjord et al.*, 2015; *Reistad et al.*, 2021]. The  
 369  $B_y$ -effect in 1.4 keV electron precipitation seen in the summer hemisphere would then  
 370 be explained by dawn or dusk magnetic field lines convecting at higher latitudes depend-  
 371 ing on the sign of  $B_y$  [*Tenfjord et al.*, 2015]. Enhanced conductivity due to increased so-  
 372 lar illumination on these field lines in turn allow stronger FACs [*Green et al.*, 2009] (and  
 373 thus particle precipitation). However, all different precipitation mechanisms are mixed  
 374 in the statistical patterns derived in this paper. Therefore, without further studies we  
 375 cannot make strong conclusions on how IMF  $B_y$  modulates different precipitation mech-  
 376 anisms, especially at low ( $< 6$  keV) energies.

377 We calculated the total energy flux and average energy of precipitating electrons  
 378 and derived ionospheric conductances from these parameters using the Robinson formu-  
 379 las. Our results show that IMF  $B_y$  indeed affects the ionospheric conductance, especially  
 380 in the dawn sector where the Hall conductance is greater for opposite signs of  $B_y$  and  
 381  $\Psi$  (the difference being about 5 Siemens during moderate solar wind driving  $d\Phi/dt/\langle d\Phi/dt \rangle$ ).  
 382 Similar results were found by *Weimer and Edwards* [2021] using an ionospheric data as-

383 simulation method, and by *Carter et al.* [2020] for the dayside NH summer Hall conduc-  
 384 tances using DMSP SSUSI measurements.

385 Our results contribute also toward understanding the physics behind IMF  $B_y$  de-  
 386 pendence of the westward electrojet, which was found already by *Friis-Christensen and*  
 387 *Wilhelm* [1975] using ground magnetometers in Greenland. Later studies based on polar-  
 388 orbiting satellites [*Friis-Christensen et al.*, 2017; *Smith et al.*, 2017; *Workayehu et al.*,  
 389 2021] and the AL index [*Holappa and Mursula*, 2018] have quantified this  $B_y$  dependence  
 390 in more detail and found that the NH westward electrojet is about 40-50% stronger for  
 391 negative tilt and positive IMF  $B_y$ . However, the NH westward electrojet shows a much  
 392 weaker  $B_y$  dependence during positive tilt (NH summer). This summer-winter difference  
 393 may be related to seasonal variation of ionospheric conductivity. The IMF  $B_y$  depen-  
 394 dence of conductance (through particle precipitation) quantified above is relatively more  
 395 significant in the dark winter hemisphere while in the summer hemisphere conductance  
 396 is also affected by sunlight. The  $B_y$  dependence of conductance could explain why the  
 397 westward electrojet is modulated strongly by IMF  $B_y$  in the winter hemisphere, but only  
 398 weakly in the summer hemisphere [*Holappa and Mursula*, 2018]. This effect is possibly  
 399 more significant at dawn than close to midnight, where the auroral oval is less sensitive  
 400 to seasonal changes in solar irradiation [*Laundal et al.*, 2018].

401 Considering the modern auroral precipitation models, our results show the impor-  
 402 tance of the combined effects of IMF  $B_y$  and  $\Psi$  into future precipitation models. That  
 403 is, dependence on  $B_y$  polarity and  $\Psi$  should be added and the two hemispheres should  
 404 be treated separately. Understandably, current precipitation models combine both hemi-  
 405 spheres for the best data coverage [*Newell et al.*, 2014; *Zhu et al.*, 2021]. However, this  
 406 artificially reduces the  $B_y$  dependence and dawn-dusk asymmetries found in this paper.  
 407 For doing this, it will be important to include all possible particle measurements from  
 408 different satellites for accurate quantification of  $B_y$  dependence in the future models.

## 409 5 Conclusions

410 We used electron precipitation measurements of the DMSP SSJ instruments from  
 411 years 1995-2022. The data was spatially binned into precipitation maps, and sorted for  
 412 steady solar wind flow (normalized Newell coupling function  $1 < d\Phi/dt / \langle d\Phi/dt \rangle < 2$ ),  
 413 positive ( $> 2$  nT) and negative ( $< -2$  nT) IMF  $B_y$  polarity, and for times of large Earth's

414 dipole tilt angle ( $\Psi > 15^\circ$  and  $\Psi < -15^\circ$ ). We showed that for fixed solar wind driv-  
 415 ing, the IMF  $B_y$  and the Earth's dipole tilt angle  $\Psi$  together modulate the auroral elec-  
 416 tron precipitation (1-30 keV) in the following way:

417 1. The dawn sector precipitation increases for opposite signs of IMF  $B_y$  and  $\Psi$  at  
 418 auroral latitudes for energies between 13.9-30 keV in both hemispheres. However, the  
 419  $B_y$  dependence is more pronounced in the summer hemisphere.

420 2. In NH summer ( $\Psi > 15^\circ$ ), the auroral precipitation shows a clear  $B_y$  depen-  
 421 dence for energies 1.4-6.5 keV. Precipitation was found to increase on the dawnside for  
 422 negative  $B_y (< -2$  nT) and on the duskside for positive  $B_y (> 2$  nT). This  $B_y$ -effect ex-  
 423 tends to higher latitudes with decreasing energies.

424 3. In SH summer ( $\Psi < -15^\circ$ ), precipitation was found to increase on the dawn-  
 425 side for positive  $B_y (> 2$  nT) and on the duskside for negative  $B_y (< -2$  nT), correspond-  
 426 ingly.

427 4. In the summer hemisphere, precipitation patterns of energies 1.4-3 keV exhibit  
 428 strong dawn-dusk asymmetries, controlled by the sign of IMF  $B_y$ .

429 5. In the NH, the average energy of the precipitation increases on the dawnside for  
 430 opposite signs of  $B_y$  and  $\Psi$ .

431 We also showed that the opposite signs of  $B_y$  and  $\Psi$  increase the Hall conductance  
 432 of the NH ionosphere. This  $B_y$  effect occurs at slightly higher latitudes in NH summer  
 433 than in NH winter.

434 Our results emphasize the need to include the effect of  $B_y$  and  $\Psi$  in future auro-  
 435 ral precipitation models. Thus, more data of auroral precipitation are needed to main-  
 436 tain large enough data coverage after sorting the data by  $B_y$  polarity, season, and for  
 437 separate hemispheres to include the explicit  $B_y$  dependence.

## 438 Open Research

439 The DMSP data was downloaded from the CEDAR Madrigal database (<http://cedar.openmadrigal.org>).  
 440 The solar wind data was downloaded from the OMNI2 database (<http://omniweb.gsfc.nasa.gov/>).

441 **Acknowledgments**

442 We acknowledge the support by the Kvantum Institute of the University of Oulu (ICONIC  
443 project). HV was supported by the Academy of Finland project 354521.

444 **References**

- 445 Anderson, B. J., H. Korth, C. L. Waters, D. L. Green, and P. Stauning (2008), Sta-  
446 tistical Birkeland current distributions from magnetic field observations by the  
447 Iridium constellation, *Annales Geophysicae*, *26*(3), 671–687, doi:10.5194/angeo-26-  
448 671-2008.
- 449 Carter, J. A., S. E. Milan, L. J. Paxton, B. J. Anderson, and J. Gjerloev (2020),  
450 Height-Integrated Ionospheric Conductances Parameterized By Interplanetary  
451 Magnetic Field and Substorm Phase, *Journal of Geophysical Research: Space*  
452 *Physics*, *125*(10), e2020JA028121, doi:https://doi.org/10.1029/2020JA028121,  
453 e2020JA028121 10.1029/2020JA028121.
- 454 Chisham, G., M. Lester, S. E. Milan, M. P. Freeman, W. A. Bristow, A. Grocott,  
455 K. A. McWilliams, J. M. Ruohoniemi, T. K. Yeoman, P. L. Dyson, R. A. Green-  
456 wald, T. Kikuchi, M. Pinnock, J. P. S. Rash, N. Sato, G. J. Sofko, J.-P. Villain,  
457 and A. D. M. Walker (2007), A decade of the Super Dual Auroral Radar Net-  
458 work (SuperDARN): scientific achievements, new techniques and future directions,  
459 *Surveys in Geophysics*, *28*, 33–109, doi:https://doi.org/10.1007/s10712-007-9017-8.
- 460 Cowley, S. (1981), Magnetospheric asymmetries associated with the y-  
461 component of the IMF, *Planetary and Space Science*, *29*(1), 79–96, doi:  
462 https://doi.org/10.1016/0032-0633(81)90141-0.
- 463 Dungey, J. W. (1961), Interplanetary Magnetic Field and the Auroral Zones, *Phys.*  
464 *Rev. Lett.*, *6*, 47–48, doi:10.1103/PhysRevLett.6.47.
- 465 Friis-Christensen, E., and J. Wilhjelm (1975), Polar cap currents for dif-  
466 ferent directions of the interplanetary magnetic field in the Y-Z plane,  
467 *Journal of Geophysical Research (1896-1977)*, *80*(10), 1248–1260, doi:  
468 https://doi.org/10.1029/JA080i010p01248.
- 469 Friis-Christensen, E., C. Finlay, M. Hesse, and K. Laundal (2017), Magnetic field  
470 perturbations from currents in the dark polar regions during quiet geomagnetic  
471 conditions, *Space Science Reviews*, *206*(1-4), 281–297.

- 472 Green, D. L., C. L. Waters, B. J. Anderson, and H. Korth (2009), Seasonal and  
473 interplanetary magnetic field dependence of the field-aligned currents for both  
474 Northern and Southern Hemispheres, *Annales Geophysicae*, *27*(4), 1701–1715,  
475 doi:10.5194/angeo-27-1701-2009.
- 476 Hardy, D. A., M. S. Gussenhoven, and E. Holeman (1985), A statistical model of  
477 auroral electron precipitation, *Journal of Geophysical Research: Space Physics*,  
478 *90*(A5), 4229–4248, doi:https://doi.org/10.1029/JA090iA05p04229.
- 479 Hardy, D. A., E. G. Holeman, W. J. Burke, L. C. Gentile, and K. H. Bounar  
480 (2008), Probability distributions of electron precipitation at high magnetic  
481 latitudes, *Journal of Geophysical Research: Space Physics*, *113*(A6), doi:  
482 https://doi.org/10.1029/2007JA012746.
- 483 Holappa, L., and K. Mursula (2018), Explicit IMF By Dependence in High-Latitude  
484 Geomagnetic Activity, *Journal of Geophysical Research: Space Physics*, *123*(6),  
485 4728–4740, doi:https://doi.org/10.1029/2018JA025517.
- 486 Holappa, L., T. Asikainen, and K. Mursula (2020), Explicit IMF Dependence in Ge-  
487 omagnetic Activity: Modulation of Precipitating Electrons, *Geophysical Research*  
488 *Letters*, *47*(4), e2019GL086676, doi:https://doi.org/10.1029/2019GL086676,  
489 e2019GL086676 10.1029/2019GL086676.
- 490 Holappa, L., R. M. Robinson, A. Pulkkinen, T. Asikainen, and K. Mursula (2021),  
491 Explicit IMF By-Dependence in Geomagnetic Activity: Quantifying Ionospheric  
492 Electrodynamics, *Journal of Geophysical Research: Space Physics*, *126*(4),  
493 e2021JA029202, doi:https://doi.org/10.1029/2021JA029202, e2021JA029202  
494 2021JA029202.
- 495 Korth, H., Y. Zhang, B. J. Anderson, T. Sotirelis, and C. L. Waters (2014), Statis-  
496 tical relationship between large-scale upward field-aligned currents and electron  
497 precipitation, *Journal of Geophysical Research: Space Physics*, *119*(8), 6715–6731,  
498 doi:https://doi.org/10.1002/2014JA019961.
- 499 Laundal, K. M., C. C. Finlay, N. Olsen, and J. P. Reistad (2018), Solar Wind and  
500 Seasonal Influence on Ionospheric Currents From Swarm and CHAMP Mea-  
501 surements, *Journal of Geophysical Research: Space Physics*, *123*(5), 4402–4429,  
502 doi:https://doi.org/10.1029/2018JA025387.
- 503 Li, W., R. M. Thorne, V. Angelopoulos, J. Bortnik, C. M. Cully, B. Ni, O. LeContel,  
504 A. Roux, U. Auster, and W. Magnes (2009), Global distribution of whistler-mode

- 505 chorus waves observed on the THEMIS spacecraft, *Geophysical Research Letters*,  
506 *36*(9), doi:<https://doi.org/10.1029/2009GL037595>.
- 507 Li, W., R. M. Thorne, J. Bortnik, Y. Nishimura, V. Angelopoulos, L. Chen, J. P.  
508 McFadden, and J. W. Bonnell (2010), Global distributions of suprathermal  
509 electrons observed on THEMIS and potential mechanisms for access into the  
510 plasmasphere, *Journal of Geophysical Research: Space Physics*, *115*(A12), doi:  
511 <https://doi.org/10.1029/2010JA015687>.
- 512 McGranaghan, R., D. J. Knipp, T. Matsuo, H. Godinez, R. J. Redmon, S. C.  
513 Solomon, and S. K. Morley (2015), Modes of high-latitude auroral conductance  
514 variability derived from DMSP energetic electron precipitation observations:  
515 Empirical orthogonal function analysis, *Journal of Geophysical Research: Space*  
516 *Physics*, *120*(12), 11,013–11,031, doi:<https://doi.org/10.1002/2015JA021828>.
- 517 McGranaghan, R. M., J. Ziegler, T. Bloch, S. Hatch, E. Camporeale, K. Lynch,  
518 M. Owens, J. Gjerloev, B. Zhang, and S. Skone (2021), Toward a Next Generation  
519 Particle Precipitation Model: Mesoscale Prediction Through Machine Learning (a  
520 Case Study and Framework for Progress), *Space Weather*, *19*(6), e2020SW002,684,  
521 doi:<https://doi.org/10.1029/2020SW002684>, e2020SW002684 2020SW002684.
- 522 Newell, P. T., T. Sotirelis, K. Liou, C.-I. Meng, and F. J. Rich (2007), A nearly  
523 universal solar wind-magnetosphere coupling function inferred from 10 magneto-  
524 spheric state variables, *Journal of Geophysical Research: Space Physics*, *112*(A1),  
525 doi:<https://doi.org/10.1029/2006JA012015>.
- 526 Newell, P. T., T. Sotirelis, and S. Wing (2009), Diffuse, monoenergetic, and broad-  
527 band aurora: The global precipitation budget, *Journal of Geophysical Research:*  
528 *Space Physics*, *114*(A9), doi:<https://doi.org/10.1029/2009JA014326>.
- 529 Newell, P. T., K. Liou, Y. Zhang, T. Sotirelis, L. J. Paxton, and E. J.  
530 Mitchell (2014), OVATION Prime-2013: Extension of auroral precipita-  
531 tion model to higher disturbance levels, *Space Weather*, *12*(6), 368–379, doi:  
532 <https://doi.org/10.1002/2014SW001056>.
- 533 Ohma, A., J. P. Reistad, and S. M. Hatch (2021), Modulation of Magne-  
534 topheric Substorm Frequency: Dipole Tilt and IMF By Effects, *Jour-*  
535 *nal of Geophysical Research: Space Physics*, *126*(3), e2020JA028,856, doi:  
536 <https://doi.org/10.1029/2020JA028856>, e2020JA028856 2020JA028856.

- 537 Ohtani, S., S. Wing, P. T. Newell, and T. Higuchi (2010), Locations of night-side  
 538 precipitation boundaries relative to R2 and R1 currents, *Journal of Geophysical*  
 539 *Research: Space Physics*, *115*(A10), doi:<https://doi.org/10.1029/2010JA015444>.
- 540 Redmon, R. J., W. F. Denig, L. M. Kilcommons, and D. J. Knipp (2017),  
 541 New DMSP database of precipitating auroral electrons and ions, *Jour-*  
 542 *nal of Geophysical Research: Space Physics*, *122*(8), 9056–9067, doi:  
 543 <https://doi.org/10.1002/2016JA023339>.
- 544 Reistad, J. P., K. M. Laundal, A. Ohma, T. Moretto, and S. E. Milan  
 545 (2020), An Explicit IMF B Dependence on Solar Wind-Magnetosphere  
 546 Coupling, *Geophysical Research Letters*, *47*(1), e2019GL086,062, doi:  
 547 <https://doi.org/10.1029/2019GL086062>, e2019GL086062 10.1029/2019GL086062.
- 548 Reistad, J. P., K. M. Laundal, N. Østgaard, A. Ohma, A. G. Burrell, S. M. Hatch,  
 549 S. Haaland, and E. G. Thomas (2021), Quantifying the Lobe Reconnection  
 550 Rate During Dominant IMF By Periods and Different Dipole Tilt Orientations,  
 551 *Journal of Geophysical Research: Space Physics*, *126*(11), e2021JA029,742, doi:  
 552 <https://doi.org/10.1029/2021JA029742>, e2021JA029742 2021JA029742.
- 553 Robinson, R. M., R. R. Vondrak, K. Miller, T. Dabbs, and D. Hardy (1987), On  
 554 calculating ionospheric conductances from the flux and energy of precipitating  
 555 electrons, *Journal of Geophysical Research: Space Physics*, *92*(A3), 2565–2569,  
 556 doi:<https://doi.org/10.1029/JA092iA03p02565>.
- 557 Sergeev, V., N. Stepanov, Y. Ogawa, S. Käki, and K. Kauristie (2018), So-  
 558 lar wind dependence of electric conductances and currents in the auroral  
 559 zone, *Journal of Atmospheric and Solar-Terrestrial Physics*, *177*, 38–45, doi:  
 560 <https://doi.org/10.1016/j.jastp.2017.07.006>, dynamics of the Sun-Earth System:  
 561 Recent Observations and Predictions.
- 562 Smith, A. R. A., C. D. Beggan, S. Macmillan, and K. A. Whaler (2017), Climatol-  
 563 ogy of the Auroral Electrojets Derived From the Along-Track Gradient of Mag-  
 564 netic Field Intensity Measured by POGO, Magsat, CHAMP, and Swarm, *Space*  
 565 *Weather*, *15*(10), 1257–1269, doi:<https://doi.org/10.1002/2017SW001675>.
- 566 Sugino, M., R. Fujii, S. Nozawa, S. C. Buchert, H. J. Opgenoorth, and A. Brekke  
 567 (2002), Relative contribution of ionospheric conductivity and electric field to iono-  
 568 spheric current, *Journal of Geophysical Research: Space Physics*, *107*(A10), SIA  
 569 20–1–SIA 20–15, doi:<https://doi.org/10.1029/2001JA007545>.

- 570 Tenfjord, P., N. Østgaard, K. Snekvik, K. M. Laundal, J. P. Reistad, S. Haaland,  
571 and S. E. Milan (2015), How the IMF By induces a By component in the closed  
572 magnetosphere and how it leads to asymmetric currents and convection patterns  
573 in the two hemispheres, *Journal of Geophysical Research: Space Physics*, *120*(11),  
574 9368–9384, doi:<https://doi.org/10.1002/2015JA021579>.
- 575 Thorne, R. M., B. Ni, X. Tao, R. B. Horne, and N. P. Meredith (2010), Scattering  
576 by chorus waves as the dominant cause of diffuse auroral precipitation, *Nature*,  
577 *467*(7318), 943–946.
- 578 Tsurutani, B. T., and E. J. Smith (1974), Postmidnight chorus: A substorm phe-  
579 nomenon, *Journal of Geophysical Research (1896-1977)*, *79*(1), 118–127, doi:  
580 <https://doi.org/10.1029/JA079i001p00118>.
- 581 Weimer, D., and T. Edwards (2021), Testing the electrodynamic method to derive  
582 height-integrated ionospheric conductances, *Annales Geophysicae*, *39*(1), 31–51,  
583 doi:10.5194/angeo-39-31-2021.
- 584 Weimer, D. R. (2001), Maps of ionospheric field-aligned currents as a function  
585 of the interplanetary magnetic field derived from dynamics explorer 2 data,  
586 *Journal of Geophysical Research: Space Physics*, *106*(A7), 12,889–12,902, doi:  
587 <https://doi.org/10.1029/2000JA000295>.
- 588 Wing, S., M. Gkioulidou, J. R. Johnson, P. T. Newell, and C.-P. Wang  
589 (2013), Auroral particle precipitation characterized by the substorm cycle,  
590 *Journal of Geophysical Research: Space Physics*, *118*(3), 1022–1039, doi:  
591 <https://doi.org/10.1002/jgra.50160>.
- 592 Workayehu, A. B., H. Vanhamäki, A. T. Aikio, and S. G. Shepherd (2021), Ef-  
593 fect of Interplanetary Magnetic Field on Hemispheric Asymmetry in Iono-  
594 spheric Horizontal and Field-Aligned Currents During Different Seasons, *Jour-  
595 nal of Geophysical Research: Space Physics*, *126*(10), e2021JA029,475, doi:  
596 <https://doi.org/10.1029/2021JA029475>, e2021JA029475 2021JA029475.
- 597 Zhu, Q., Y. Deng, A. Maute, L. M. Kilcommons, D. J. Knipp, and M. Hairston  
598 (2021), ASHLEY: A New Empirical Model for the High-Latitude Electron  
599 Precipitation and Electric Field, *Space Weather*, *19*(5), e2020SW002,671, doi:  
600 <https://doi.org/10.1029/2020SW002671>, e2020SW002671 2020SW002671.